ELSEVIER

Fusion Engineering and Design 42 (1998) 307–318

Fusion Engineering and Design

Experimental measurement of nuclear heating in a graphite-cantered assembly in deuterium–tritium neutron environment for the validation of data and calculation

Anil Kumar [a,*], Yujiro Ikeda [b], Mahmoud Z. Youssef [a], Mohamed A. Abdou [a], Fujio Maekawa [b], Yoshimi Kasugai [b]

[a] *School of Engineering and Applied Science, University of California (UCLA), Los Angeles, CA 90095-159710, USA*
[b] *Department of Reactor Engineering, Japan Atomic Energy Research Institute, Tokai, Ibaraki, 319-11, Japan*

Abstract

Within the framework of the ITER Task T-218 entitled 'Shielding Blanket Neutronics Experiments', nuclear heating measurements were conducted jointly by the USA and Japan using a micro calorimetric technique in a graphite-cantered assembly. An accelerator-based D–T neutron source at JAERI was used to provide a mixed neutron and photon field. The first measurements related to direct micro calorimetric measurements in individual graphite probes along the axis. In the second set, the first graphite probe was replaced, one by one, by single probes of beryllium, aluminum, silicon, silicon carbide, titanium, vanadium, chromium, iron, stainless steel 316, nickel, copper, zirconium, niobium, molybdenum, tungsten. Analysis of the measurements has been carried out using Monte Carlo code MCNP with FENDL-1, ENDF/B-VI and MCPLIB nuclear data libraries. A comparison of calculations (C) and experiments (E) shows a C/E ratio lying in a C/E band extending from 0.9 to 1.2 for beryllium, graphite, copper, chromium, iron, nickel, 316 stainless steel, titanium, vanadium, molybdenum, niobium and tungsten. However, larger deviations from unity are seen for C/E values for silicon, zirconium, and aluminum. Though FENDL-1 and ENDF/B-VI libraries provide very close nuclear heating rates for most of the probe materials, significant divergences are seen for silicon, silicon carbide, aluminum, titanium, zirconium, niobium, and molybdenum. The divergences are traceable to differences in neutron kerma factors as well as gamma production cross-sections of these materials.

1. Introduction

Nuclear heating measurements were conducted jointly by the USA and Japan using a micro calorimetric technique in a graphite-cantered assembly, as a sub-task of ITER Task T-218 entitled 'Shielding Blanket Neutronics Experiments'. The key idea behind this effort has been in compiling an experimental database for directly measured nuclear heating rates, on one hand, and, their use in validation of calculations, on the other [1–5]. An accelerator-based D–T neutron source at JAERI, with a nominal intensity of 5×10^{12} s^{-1}, provided neutrons. The first measurements related to direct micro calorimetric measurements in individual graphite probes along

* Corresponding author.

0920-3796/98/$19.00
PII S0920-3796(97)00155-5

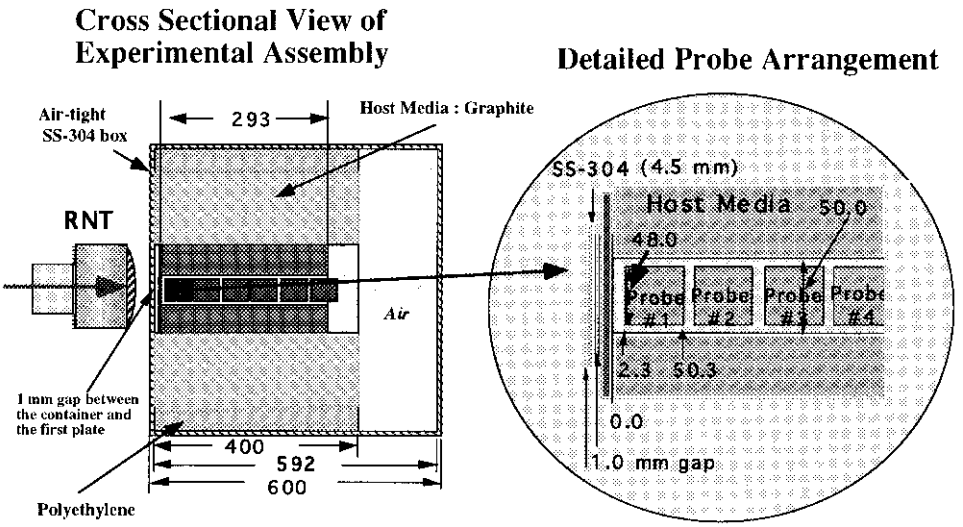

Fig. 1. Schematic representation of graphite-cantered experimental assembly.

the axis. In the second set, the first graphite probe was replaced, one by one, by single probes of beryllium, aluminum, silicon, silicon carbide, titanium, vanadium, chromium, iron, stainless steel 316, nickel, copper, zirconium, niobium, molybdenum, tungsten. Sets of TLD's were irradiated in a separate set of experiments in this assembly to receive information on gamma heating component alone. In addition, sets of dosimetric foils were irradiated at various locations in the central region to monitor the neutron energy spectrum.

Analysis of the nuclear heating measurements has been carried out and calculations were compared to the experimental measurements. For the majority of materials, the ratio of calculation (C) to experimental measurement (E) lies in a broad band spanning from 0.9 to 1.2. Significant divergences from this behavior are, however, seen for silicon, zirconium and aluminum.

2. Experiments

A micro-calorimetric technique employing small probes of various materials was previously developed and applied for direct measurement of total nuclear heating, deposited by neutrons and induced photons [1–4]. In the current series of experiments, the same technique has been applied to measure nuclear heating in probes of various materials retained inside a graphite-cantered assembly. A schematic representation of the assembly is provided in Fig. 1. Experimental assembly consisted of a central graphite region of ~ 30 cm in length. It was made up of cylindrical graphite probes, measuring 48 mm in diameter by 48 mm in length each. This region was enveloped by a ~ 22.5 cm thick graphite shell and a 5 cm thick polyethylene layer. All of these components of the assembly were stacked in a 4 mm thick stainless steel container of external dimensions that measured $600 \times 600 \times 600$ mm. The experimental assembly was kept directly in front of the rotating target D–T neutron source at JAERI, at a distance of 14 mm. The first measurements related to direct micro calorimetric measurements in individual graphite probes along the axis. In the second set of measurements, the first graphite probe was replaced, one by one, by single probes of beryllium, aluminum, silicon, silicon carbide, titanium, vanadium, chromium, iron, stainless steel 316, nickel, copper, zirconium, niobium, molybdenum, tungsten. Sets of TLD's were irradiated in a separate series of experiments in this assembly to receive information on gamma heating component alone. The TLD's were attached to the front

and the rear end of each of the six graphite probes in the experiments with the reference assembly. Similarly, in the experiments with foreign probes replacing the first graphite probe, a set each of TLD's was attached to both the front and the rear ends of the foreign probe.

Table 1
Information on nuclear heating experiments in graphite-centered assembly

Assembly	Graphite-centered
Neutron source	Rotating target D–T neutron source at FNS, JAERI
Source neutron intensity	3×10^{12} s^{-1}
Experimental locations	1st–6th graphite probes (blocks) in the central graphite region 1st graphite probe replaced by a foreign probe material
Source exposure periods	3, 5 min per pulse
Probe materials	Be, C, Al, Si, SiC, Ti, V, Cr, Fe, Ni, 316 stainless steel, Cu, Zr, Nb, Mo, W
Measurement techniques	Calorimetry (total heating), TLD (gamma ray heating), foil activation (reaction rates)
Experimental error	Less than 10% on all foreign probes More for the 4th–6th graphite probes

Table 2
Dimensions and heat capacity of nuclear heating probes

Probe material	Dimensions (mm × mm)	Heat capacity (J/g/K)
Ti	$\phi48\times$H50	0.521
Al	$\phi48\times$H50	0.903
C	$\phi48\times$H48	0.711
V	$\phi48\times$H48	0.490
SiC	$\phi48.2\times$H48.3	0.712
Si	$\phi47.9\times$H48	0.712
Be	$\phi48\times$H48	1.824
Ni	$\phi48\times$H48	0.444
Zr	$\phi48\times$H48	0.279
W	$\phi48\times$H48	0.132
Mo	$448\times$H48	0.248
Nb	$\phi48\times$H48	0.266
Fe	$\phi48\times$H48	0.449
Cr	$\phi30\times$H30	0.447
SS316	$\phi48\times$H48	0.445
Cu	$\phi48\times$H48	0.385

Sets of dosimetric foils of Al, Nb, In and Au were irradiated at locations in between the graphite probes all along the central graphite channel in the reference assembly.

In so far as micro-calorimetric measurements are concerned, a thermistor each was implanted in the front and rear ends of the first two graphite probes, and only at the front ends of the remaining graphite probes. With the foreign probes, both the front and rear end thermistors were utilized. Two kinds of thermistors of 5 KΩ and 10 KΩ resistance at 25°C were used. The temperature coefficient of these thermistors was $\sim$0.044°K at 25°C. Usually, a cycle length of 10 s is kept for reading off thermistors' resistances by model 182 sensitive digital voltmeters from Keithley Instruments. Generally, a steady current of 20 μA was circulated in all of the thermistors. As for the D–T neutron source pulsing, usually 3 pulses of 3 min each with a separation of almost 3 min were found adequate. In some instances, pulses of 5 min duration were also used. Tables 1 and 2 provide information on experimental conditions, experimental error, dimensions and heat capacity of various probe materials used in the experiments. The heat capacities were taken from [6,7]. A detailed presentation on factors impacting the accuracy of the measurements is available in [1,2].

Resistance change data for both front and rear sensors in beryllium and silicon probes is shown in Figs. 2 and 3. Note that there is very little difference between the resistance changes across the front and the rear sensors for both of the probes. This translates into the same temperature change rate for both of the sensors. A mean temperature change rate was obtained for each probe and was converted into a heating rate expressed in J/g/source neutron using the heat capacity and measured source neutron intensity as outlined in [1,2].

3. Analysis

A 3D Monte Carlo code MCNP [8] was used for modeling the experimental geometry. Two

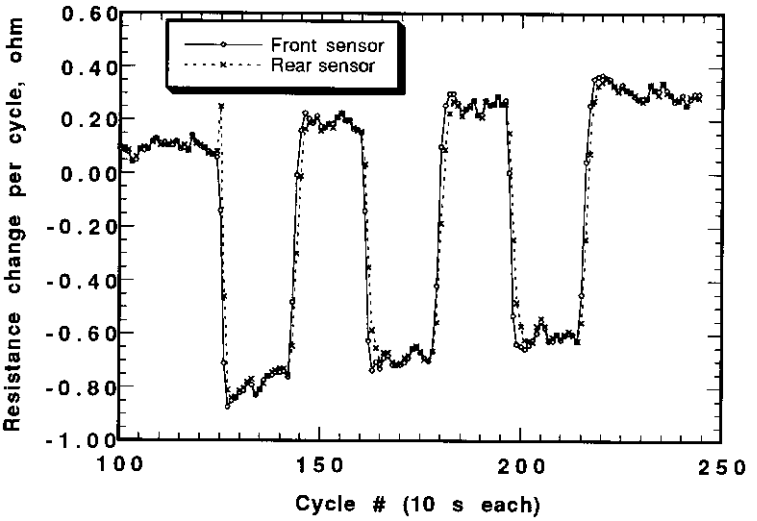

Fig. 2. Resistance change per cycle in thermistors kept in front and rear ends of a beryllium probe located in a lead location of the central graphite channel.

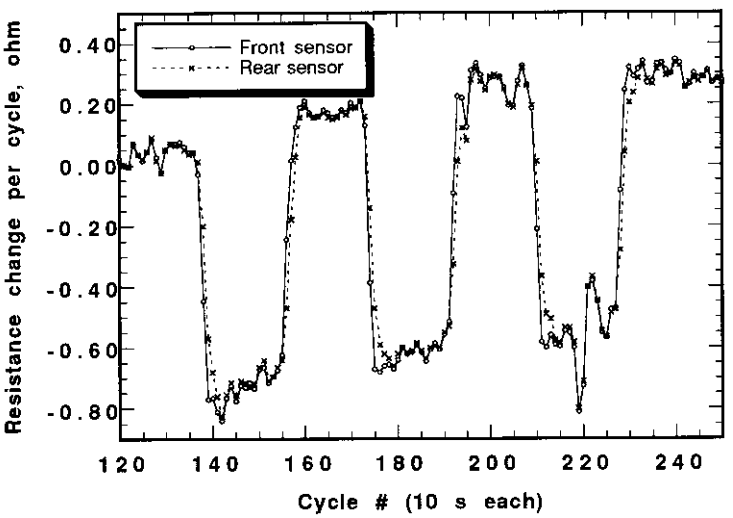

Fig. 3. Resistance change per cycle in thermistors kept in front and rear ends of a silicon probe located in a lead location of the central graphite channel.

separate sets of calculations were carried out; one with FENDL-1 library [9–11] and another with ENDF/B-VI library [8]. Both of these libraries contain cross-sections and response functions for neutron interactions and photon production. MCNP uses MCPLIB library for photon transport once a photon source is available. The nuclear heat deposition rate was averaged over the volume of a probe.

4. Results

The measured nuclear heating profile in graphite probes in the central channel is shown in Fig. 4. As expected, nuclear heating drops as one goes deeper into the assembly. The error on the measurement increases as nuclear heating drops for deeper locations and noise becomes comparable to the signal picked up by the sensitive volt-

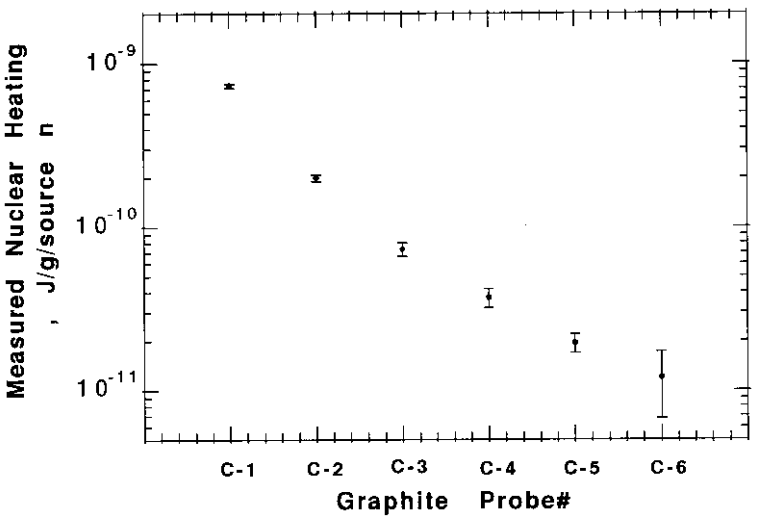

Fig. 4. Measured nuclear heating (J/g/source neutron) in all six graphite probes in the central graphite channel.

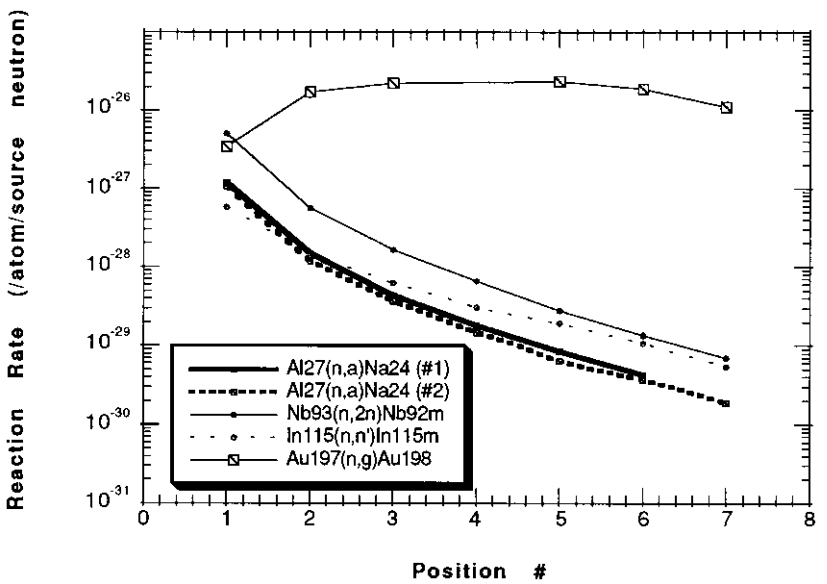

Fig. 5. Measured dosimetric reaction rate (reactions/atom/source neutron) at locations between the graphite probes in the graphite channel. First position is directly in front of the first probe.

meter. Fig. 5 has plots of measured dosimetric reaction rate profiles. The dosimetric reactions plotted include: $^{27}Al(n, \alpha)^{24}Na$, $^{93}Nb(n, 2n)^{92m}Nb$, $^{115}In(n, n')^{115m}In$, and $^{197}Au(n, \gamma)^{198}Au$. There are two plots for $^{27}Al(n, \alpha)^{24}Na$ reaction rate—plot 1 represents data from the first long irradiation and plot 2 represents data from the second long irradiation. With the exception of $^{197}Au(n, \gamma)^{198}Au$, the reaction rates drop as one looks at deeper positions inside the assembly. $^{197}Au(n, \gamma)^{198}Au$ reaction rates rise for the first three positions and then start to drop.

The ratio of calculation to experimental measurement of nuclear heating, i.e. C/E, is shown as a function of the graphite probe number in the central channel in Fig. 6. The C/E ratio lies

between 0.8 and 1.2 for the first five probes. Both FENDL-1 and ENDF/B-VI give the same results. The experimental error is too large to permit a meaningful observation for the last graphite probe. The C/E ratio for nuclear heating in various foreign probes is plotted in Fig. 7. Note that, except for silicon, zirconium, and aluminum, C/E lies between 0.9 and 1.3. As for the comparison between calculations by FENDL-1 and ENDF/B-VI, they are the same except for aluminum, silicon, silicon carbide, titanium, zirconium, niobium, and molybdenum. The largest divergences between the two libraries are seen for zirconium, aluminum, silicon, silicon carbide, and titanium. The ratio of calculation to experimental dosimetric reaction rates as a function of position is given in Fig. 8 for both libraries. C/E's for $^{27}Al(n, \alpha)^{24}Na$ are closest to unity. Whereas C/E's for $^{115}In(n, n')^{115m}In$ are significantly greater than unity, they are significantly below unity for $^{197}Au(n, \gamma)^{198}Au$. One could infer that whereas neutron energy spectrum is underpredicted in a very low energy range (as seen by $^{197}Au(n, \gamma)^{198}Au$), it is overpredicted in the intermediate energy range (as seen by $^{115}In(n, n')^{115m}In$).

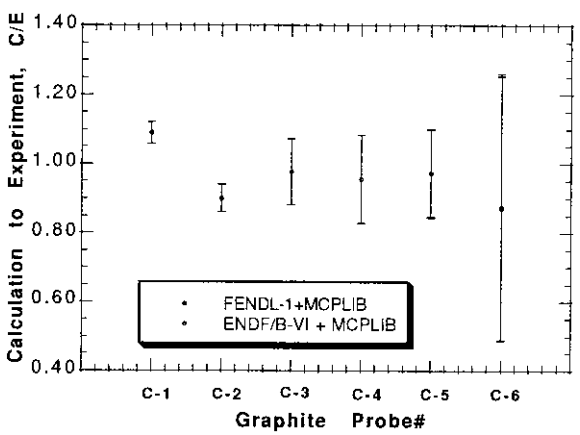

Fig. 6. The ratio of calculation to experimental measurement of total nuclear heating in graphite probes in the central channel. Two different transport and photon production cross-section libraries, i.e. FENDL-1 and ENDF/B-VI were used with MCNP. MCPLIB provided photon transport cross-section data.

5. Discussion

Fractional contributions to nuclear heating by neutrons and gamma-rays for various graphite probes are shown in Fig. 9. Both FENDL-1 and ENDF/B-VI yield the same results. One can observe the steady rise of gamma-ray heating fraction from $\sim 10\%$ in the first probe to $\sim 30\%$ in the sixth probe. Fig. 10 is a plot of fractional contributions to nuclear heating for various foreign probes—calculated with FENDL-1 library. Note that gamma fraction is generally low for low Z materials, i.e. beryllium, aluminum, but rises rapidly for high Z materials, i.e. Mo and W. The calculations with ENDF/B-VI show significant differences with those with FENDL-1 for aluminum, titanium, silicon, silicon carbide and zirconium.

Fig. 11 shows the plot of neutron kerma factor, gamma-ray kerma factor, neutron flux, and gamma-ray flux for the silicon probe as a function of particle (neutron/photon) energy, as calculated by FENDL-1 library. Notice that the gamma kerma factor is always above the neutron kerma factor. However, neutron flux is significantly above gamma-ray flux in higher energy range, but it is lower in the intermediate energy range. The combined effect of the kerma factor and flux is shown in Fig. 12, which plots nuclear heating sensitivity [2] as a function of neutron and gamma-ray energy for the silicon probe. As discussed in [2], nuclear heating sensitivity at a given energy is basically a measure of differential contribution to total nuclear heating. It is obvious that high energy neutrons overwhelm the contributions from both gamma-rays and low energy neutrons. Both FENDL-1 and ENDF/B-VI predict similar qualitative behavior, however, significant differences are apparent for both neutrons and gamma-rays.

Fig. 13 shows plots of the neutron kerma factor and the nuclear heating sensitivity for a titanium probe as a function of neutron energy. Note that the FENDL-1 kerma factor and sensitivity show large oscillations, unlike ENDF/B-VI. Fig. 14 shows gamma-ray flux and nuclear heating sensitivity as a function of gamma-ray energy for the titanium probe. It is evident that the two

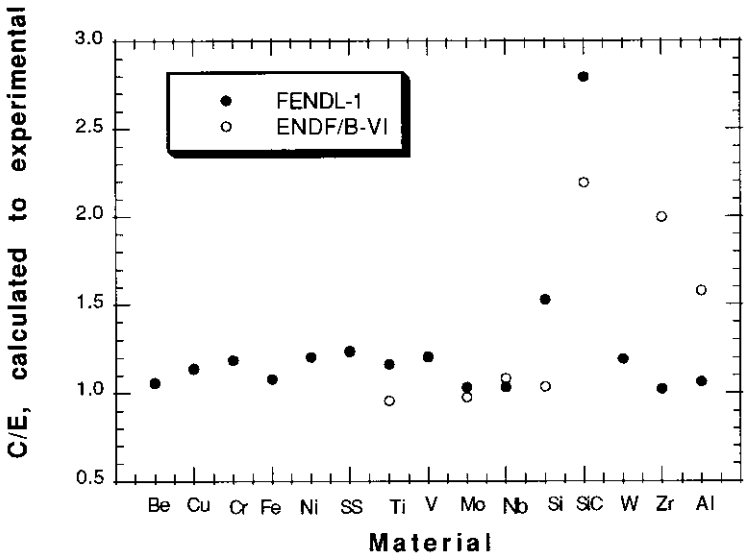

Fig. 7. The ratio of calculation to experimental measurement of total nuclear heating in foreign material probes replacing the first graphite probe in the central channel.

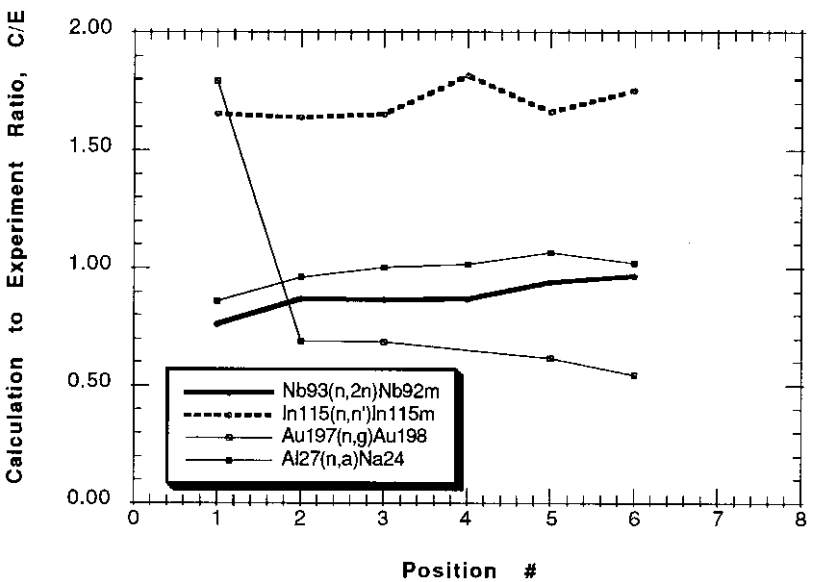

Fig. 8. The ratio of calculation to experimental measurement of dosimetric reaction rates at locations between the graphite probes in the central channel. The first position is directly in front of the first probe.

libraries have significant differences in gamma-ray production cross-sections. These differences are responsible for differences in the gamma-ray spectrum, and, hence, the gamma-ray component of nuclear heating. Thus, it follows that differences in neutron kerma factors as well as gamma-ray production cross-sections are responsible for the large differences in the nuclear heating calculations by FENDL-1 and ENDF/B-VI.

Fig. 15 shows plots of the neutron kerma factor and nuclear heating sensitivity for a zirco-

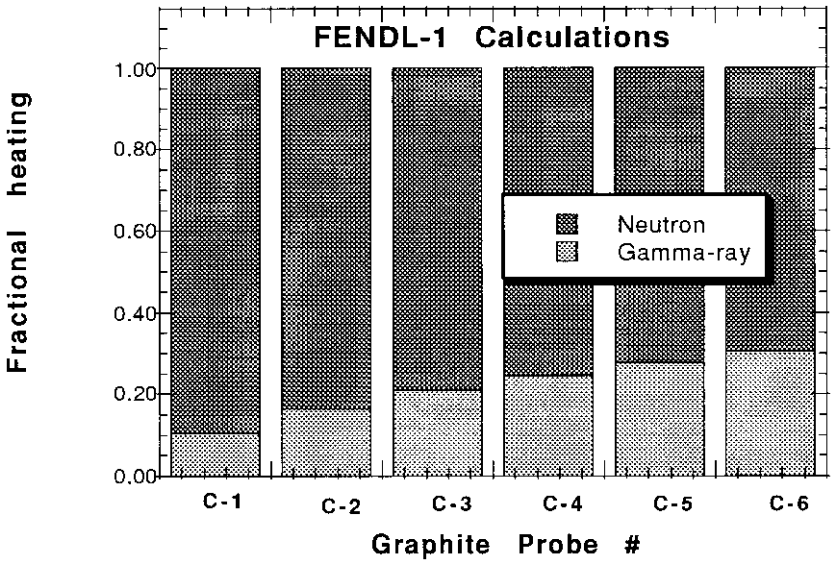

Fig. 9. The calculated fractional contributions to nuclear heating by neutrons and gamma-rays in graphite probes in the central channel.

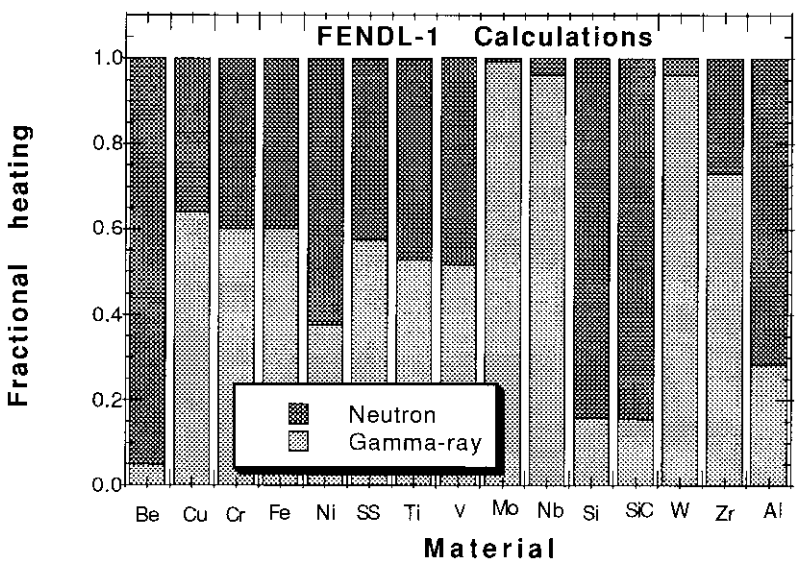

Fig. 10. The calculated fractional contributions to nuclear heating by neutrons and gamma-rays in foreign probes, replacing the first graphite probe, in the central channel.

nium probe as a function of neutron energy. Notice the 1–2 orders of magnitude difference between FENDL-1 and ENDF/B-VI kerma factors. This differences translates into a similar difference in nuclear heating sensitivity. Fig. 16 shows gamma-ray flux and nuclear heating sensitivity as a function of gamma-ray energy for the zirconium probe. Again, as also observed for titanium, the two libraries have significant differences in gamma-ray production cross-sections. As a result, the differences in neutron kerma factors as well as gamma-ray production

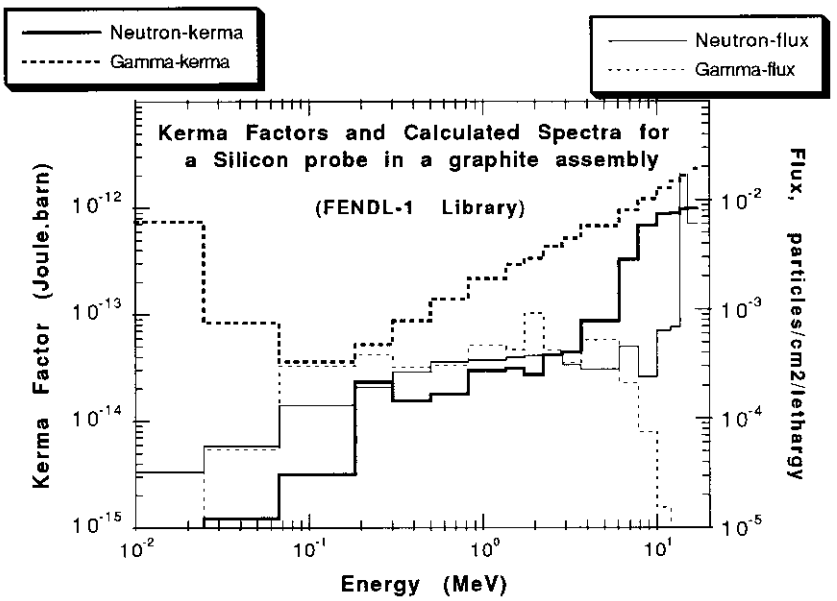

Fig. 11. The calculated neutron kerma factor (Joule.barn/atom), gamma-ray kerma factor (Joule.barn/atom), neutron flux (n/cm^2/lethargy), and gamma-ray flux (n/cm^2/lethargy) in a silicon probe as a function of particle energy (MeV).

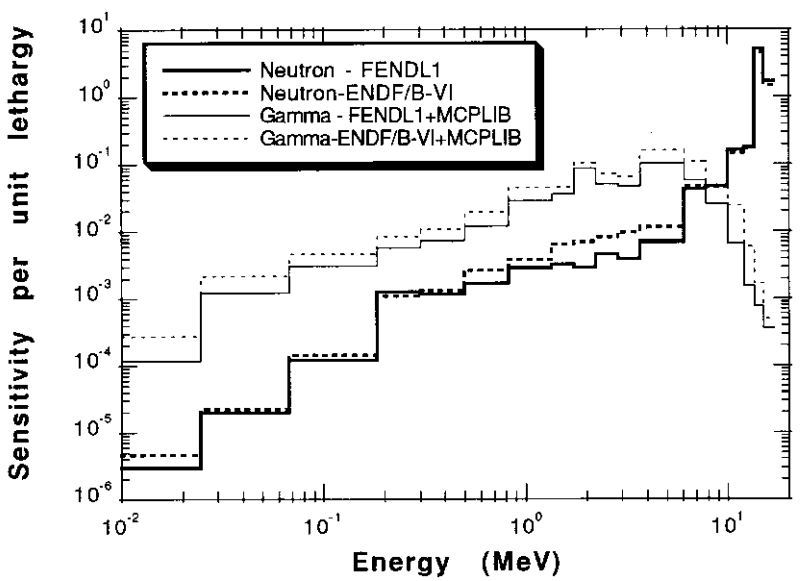

Fig. 12. Nuclear heating sensitivity—differential nuclear heating per unit lethargy—as a function of neutron and gamma-ray energy for a silicon probe in the central graphite channel.

cross-sections lead to the large differences found in the nuclear heating calculations for zirconium by FENDL-1 and ENDF/B-VI. A similar trend has been found for aluminum.

6. Conclusions

The Japan–USA collaborative work on nuclear heating experiments for ITER task T218 has been

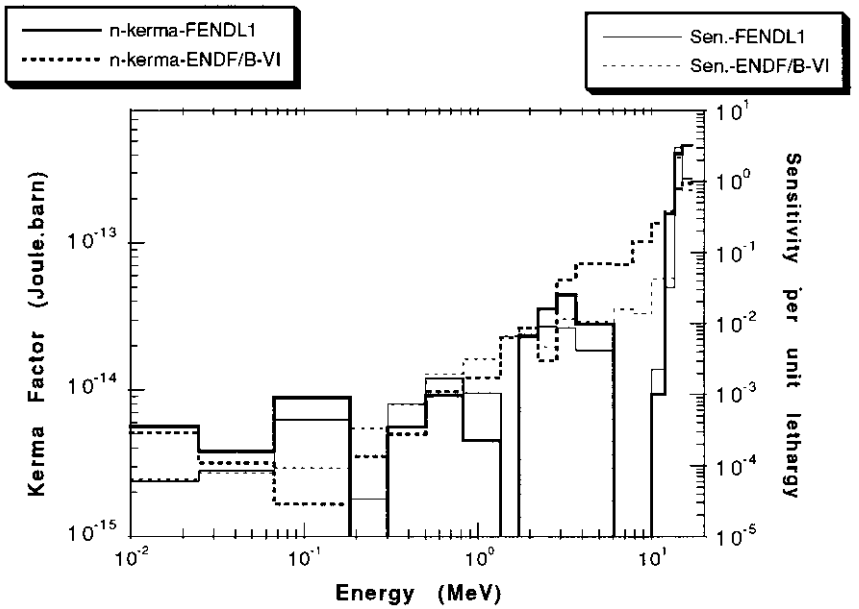

Fig. 13. Neutron kerma factor (Joule.barn/atom) and nuclear heating sensitivity of a titanium probe as a function of neutron energy (MeV) for FENDL-1 and ENDF/B-VI libraries.

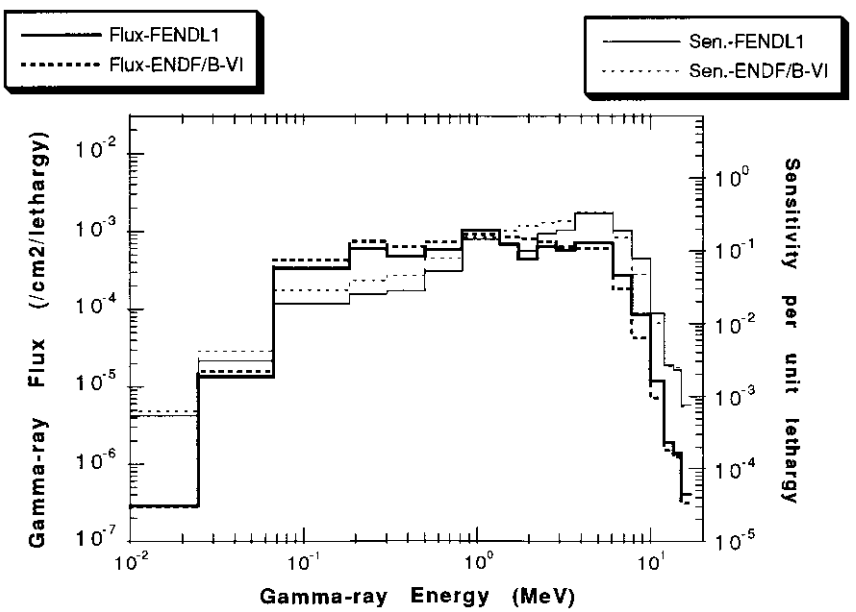

Fig. 14. Gamma-ray flux (n/cm^2/lethargy) and nuclear heating sensitivity of a titanium probe as a function of gamma-ray energy (MeV) for FENDL-1 and ENDF/B-VI libraries.

presented and discussed. Direct nuclear heating measurements have been carried out for graphite, beryllium, aluminum, silicon, silicon carbide, titanium, vanadium, chromium, iron, stainless steel 316, nickel, copper, zirconium, niobium, molybdenum and tungsten. An analysis of these measure-

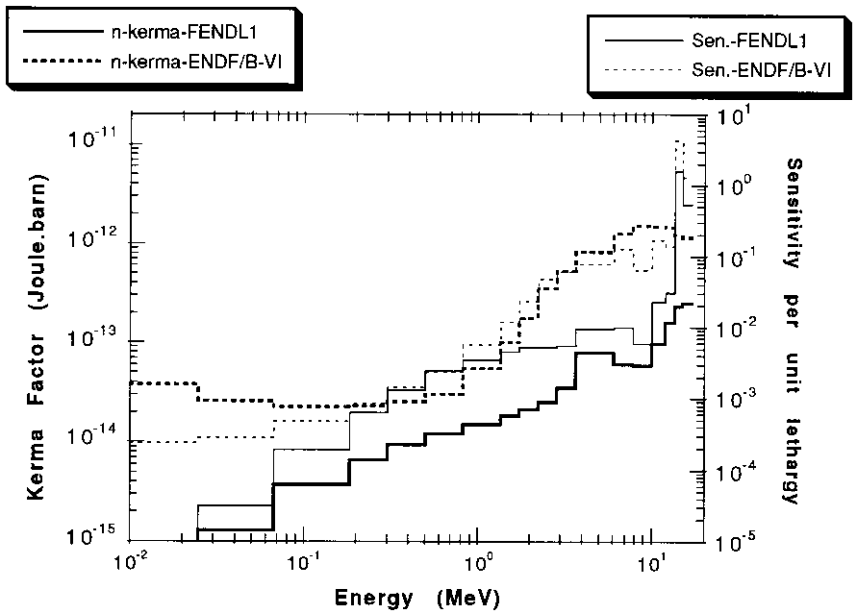

Fig. 15. Neutron kerma factor (Joule.barn/atom) and nuclear heating sensitivity of a zirconium probe as a function of neutron energy (MeV) for FENDL-1 and ENDF/B-VI libraries.

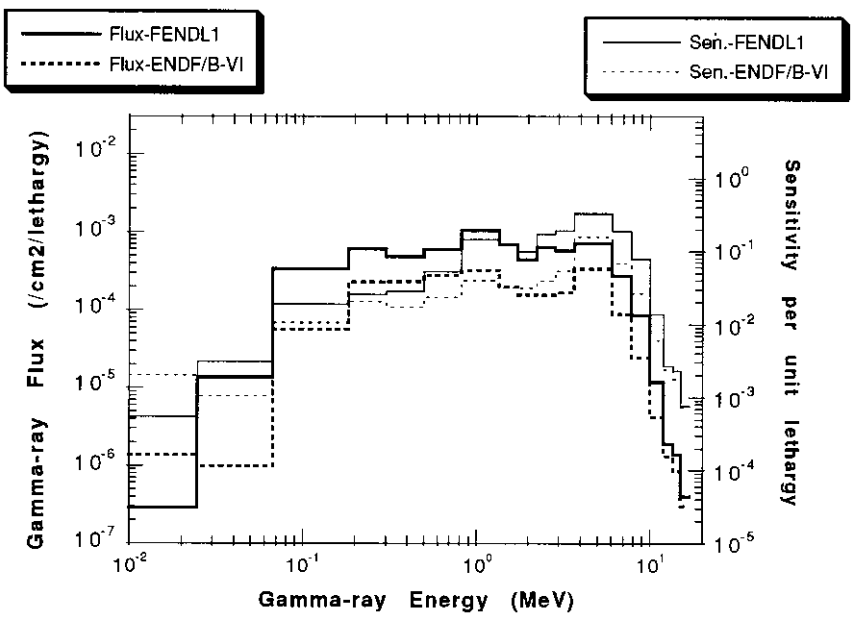

Fig. 16. Gamma-ray flux (n/cm^2/lethargy) and nuclear heating sensitivity of a zirconium probe as a function of gamma-ray energy (MeV) for FENDL-1 and ENDF/B-VI libraries.

ments was carried out using Monte Carlo code MCNP and FENDL-1 and ENDF/B-VI libraries. For the majority of the materials, the ratio of calculation (C) to experimental measurement (E) lies in a broad band spanning from 0.9 to 1.2. Significant divergences from this behavior are,

however, seen for silicon, zirconium, and aluminum.

Acknowledgements

The US contribution was supported by the US Department of Energy, Office of Fusion Energy, contract no. DE-FG03-86ER52123. This paper is an account of work assigned to the US and Japan Home Teams under Task Agreement No. T-218 within the Agreement among the European Atomic Energy Community, the Government of Japan, the Government of the Russian Federation, and the Government of the USA on Cooperation in the Engineering Design Activities for the International Thermonuclear Experimental Reactor ('ITER EDA Agreement') under the auspices of the International Atomic Agency (IAEA). The report has not been reviewed by the ITER Publications Office.

References

[1] Y. Ikeda, A. Kumar, C. Konno, K. Kosako, Y. Oyama, F. Maekawa, H. Maekawa, M.Z. Youssef, M.A. Abdou, Direct nuclear heating measurements and analyses for structural materials induced by deuterium–tritium neutrons, Fusion Technol. 28 (1995) 156.

[2] A. Kumar, Y. Ikeda, M.A. Abdou, M.Z. Youssef, C. Konno, K. Kosako, Y. Oyama, T. Nakamura, H. Maekawa, Direct nuclear heating measurements and analyses for plasma facing materials, Fusion Technol. 28 (1995) 173.

[3] A. Kumar, Y. Ikeda, M.Z. Youssef, M.A. Abdou, F. Maekawa, Y. Uno, H. Maekawa, Direct nuclear heating measurements on first wall/PFC/blanket structural materials, UCLA report no. UCLA-FNT-92/UCLA-ENG-94-42 on subtask No. 1 of ITER Task T16, Preparation of neutronic experiments and measuring techniques, December, 1994.

[4] Y. Ikeda, C. Konno, K. Kosako, Y. Oyama, F. Maekawa, H. Maekawa, A. Kumar, M.Z. Youssef, M.A. Abdou, Measurement and analysis of nuclear heat deposition in structural materials induced by D–T neutrons, Fusion Technol. 21 (1991) 2190.

[5] A. Kumar, Y. Ikeda, On disagreement between measurements and calculations of D–T neutron driven induced radioactivity and nuclear heating, Proc. Int. Conf. Nuclear Data for Science and Technology, Am. Nucl. Soc., Gatlinburg, Tennessee, 9–13 May, 1994, pp. 883–895.

[6] Y.S. Touloukian, E.H. Buyco, Specific Heat: Metallic Elements and Alloys, Vol. 4 of Series on Thermophysical Properties of Matter, IFI/Plenum, New York, 1970 (see also, by same authors, Specific Heat: Nonmetallic Solids, vol. 5 of the series).

[7] JSME Data Book: Heat Transfer, 3rd ed., Jpn. Soc. Mech. Eng., 1975.

[8] J.F. Briesmeister (Ed.), MCNP—A General Monte Carlo Code for Neutron and Photon Transport: Version 3A, report no. LA-7396-M, Rev. 2, September, 1988 (along with MCNP3B newsletter dated 18 July, 1988, Los Alamos National Laboratory).

[9] A.B. Pashchenko, Status of FENDL activation file and plans for the future developments, Proc. Int. Workshop on Nuclear Data for Fusion Reactor Technology, Del Mar, California, 3–6 May, 1993.

[10] A.B. Pashchenko, Completion of FENDL-1 and start of FENDL-2, IAEA NDC report, INDS(NDS)-325, 1996.

[11] S. Ganesan, H. Wienke, FENDL/MC-1.0 library of continuous energy cross sections in ACE format for neutron-photon transport calculations with the monte carlo neutron and photon transport code system MCNP 4A, IAEA-NDS-169, 1995.